Structural Insights into the Substrate Binding and Stereoselectivity of *Giardia* Fructose-1,6-bisphosphate Aldolase[†,‡]

Andrey Galkin,[§] Zhimin Li,[||] Ling Li,[||] Liudmila Kulakova,[§] Lipika R. Pal,[§] Debra Dunaway-Mariano,[||] and Osnat Herzberg*[,§]

W. M. Keck Laboratory for Structural Biology, Center for Advanced Research in Biotechnology, University of Maryland Biotechnology Institute, Rockville, Maryland 20850, and Department of Chemistry and Chemical Biology, University of New Mexico, Albuquerque, New Mexico 87131

Received January 25, 2009; Revised Manuscript Received February 18, 2009

ABSTRACT: *Giardia lamblia* fructose-1,6-bisphosphate aldolase (FBPA) is a member of the class II zinc-dependent aldolase family that catalyzes the cleavage of D-fructose 1,6-bisphosphate (FBP) into dihydroxyacetone phosphate (DHAP) and D-glyceraldehyde 3-phosphate (G3P). In addition to the active site zinc, the catalytic apparatus of FBPA employs an aspartic acid, Asp83 in the *G. lamblia* enzyme, which when replaced with an alanine residue renders the enzyme inactive. A comparison of the crystal structures of D83A FBPA in complex with FBP and of wild-type FBPA in the unbound state revealed a substrate-induced conformational transition of loops in the vicinity of the active site and a shift in the location of Zn^{2+}. When FBP binds, the Zn^{2+} shifts up to 4.6 Å toward the catalytic Asp83, which brings the metal within coordination distance of the Asp83 carboxylate group. In addition, the structure of wild-type FBPA was determined in complex with the competitive inhibitor D-tagatose 1,6-bisphosphate (TBP), a FBP stereoisomer. In this structure, the zinc binds in a site close to that previously seen in the structure of FBPA in complex with phosphoglycolohydroxamate, an analogue of the postulated DHAP ene-diolate intermediate. Together, the ensemble of structures suggests that the zinc mobility is necessary to orient the Asp83 side chain and to polarize the substrate for proton transfer from the FBP C(4) hydroxyl group to the Asp83 carboxyl group. In the absence of FBP, the alternative zinc position is too remote for coordinating the Asp83. We propose a modification of the catalytic mechanism that incorporates the novel features observed in the FBPA−FBP structure. The mechanism invokes coordination and coplanarity of the Zn^{2+} with the FBP's O-C(3)-C(4)-O group concomitant with coordination of the Asp83 carboxylic group. Catalysis is accompanied by movement of Zn^{2+} to a site coplanar with the O-C(2)-C(3)-O group of the DHAP. *gl*FBPA exhibits strict substrate specificity toward FBP and does not cleave TBP. The active sites of FBPAs contain an aspartate residue equivalent to Asp255 of *gl*FBPA, whereas tagatose-1,6-bisphosphate aldolase contains an alanine in this position. We and others hypothesized that this aspartic acid is a likely determinant of FBP versus TBP specificity. Replacement of Asp255 with an alanine resulted in an enzyme that possesses double specificity, now cleaving TBP (albeit with low efficacy; $k_{cat}/K_m = 80$ M^{-1} s^{-1}) while maintaining activity toward FBP at a 50-fold lower catalytic efficacy compared with that of wild-type FBPA. The collection of structures and sequence analyses highlighted additional residues that may be involved in substrate discrimination.

Members of the aldolase family catalyze retroaldol/aldol reactions that result in cleavage or formation of C−C bonds. The best-studied aldolase family member is the fructose-1,6-bisphosphate aldolase (FBPA).[1] FBPA catalyzes the reversible cleavage of D-fructose 1,6-bisphosphate (FBP) to dihydroxyacetone phosphate (DHAP) and D-glyceraldehyde 3-phosphate (G3P) [EC 4.1.2.13 (Figure 1A)], a key step of the classical Embden−Meyerhof−Parnas glycolytic pathway.

Two evolutionarily and mechanistically unrelated FBPA classes have been identified, class I (which employs an active site lysine in Schiff base formation) and class II (which employs a Zn^{2+} cofactor) (*1, 2*). The crystal structures of the class II FBPA from *Escherichia coli* (*ec*FBPA) in the apo state and in complex with the inhibitor phosphoglycolohydroxamate [PGH (Figure 1C)] have been elucidated (*3*−*5*). The class II FBPA adopts an $(\alpha/\beta)_8$-barrel fold. At the active site, the Zn^{2+} coordinates the imidazole groups of three histidine residues and the C(2)═O and N(3)OH oxygen atoms of the FGH inhibitor. The structure of the *E. coli* tagatose-1,6-bisphosphate aldolase (*ec*TBPA), a class II aldolase acting on D-tagatose 1,6-bisphosphate [TBP, the

[†] Supported by National Institutes of Health Grant RO1 AI059733.
[‡] Coordinates deposited as Protein Data Bank (PDB) entries 3GAK, 3GAY, and 3GB6.
* To whom correspondence should be addressed: Center for Advanced Research in Biotechnology, 9600 Gudelsky Dr., Rockville, MD 20850. Telephone: (240) 314-6245. Fax: (240) 314-6255. E-mail: osnat@carb.nist.gov.
[§] University of Maryland Biotechnology Institute.
[||] University of New Mexico.
[1] Abbreviations: FBPA, fructose-1,6-bisphosphate aldolase; *gl*FBPA, *Giardia* FBPA; *ec*TBPA, *Escherichia coli* tagatose-1,6-bisphosphate aldolase; *ec*FBPA, *E. coli* FBPA; PGH, phosphoglycolohydroxamate; FBP, D-fructose 1,6-bisphosphate; TBP, D-tagatose 1,6-bisphosphate; DHAP, dihydroxyacetone phosphate; G3P, D-glyceraldehyde 3-phosphate; rms, root-mean-square.

10.1021/bi9001166 CCC: $40.75
Published on Web 02/23/2009

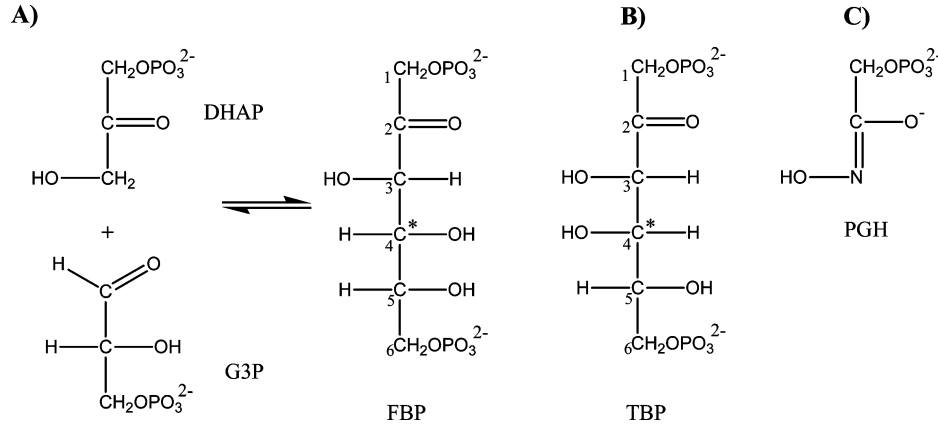

FIGURE 1: (A) Reaction catalyzed by fructose-1,6-bisphosphate aldolase (FBPA). (B) D-Tagatose 1,6-bisphosphate (TBP), a C(4) hydroxyl epimer of D-fructose 1,6-bisphosphate (FBP). (C) Phosphoglycolohydroxamate (PGH), a DHAP ene-diolate transition-state analogue.

C(4) hydroxyl epimer of FBP (Figure 1B)], has also been reported in complex with PGH (*6*), and it revealed the same Zn^{2+} coordination pattern. The structural data, together with the kinetic behavior of active site-directed mutants, led investigators to propose a model of the class II FBPA substrate recognition and catalysis in which the Zn^{2+} plays a central role (*7*−*9*).

Despite the growing knowledge of the structure and catalytic mechanism of the Zn^{2+}-dependent enzymes, the binding interactions that take place among the enzyme, cofactor, and substrate in the Michaelis complex are not fully known. Specifically, there is no structural information showing how the G3P product, or the intact hexose unit of the FBP substrate, binds to FBPA.

Giardia lamblia, a flagellated protozoan, is a disease-causing parasite in developing and developed countries. Giardiasis symptoms range from severe diarrhea, weight loss, vomiting, and malnutrition and if not treated might lead to death. Giardiasis is often difficult to treat because of increasing drug resistance, recurrence, and undesirable side effects. Previously, we reported the crystal structure and kinetic characterization of FBPA from *G. lamblia* (*gl*FBPA) (*10*). We suggested that the enzyme is a potential target for the development of new drugs against giardiasis because it is essential for *Giardia* survival and because, unlike the human and other mammalian FBPAs that belong to the class I aldolase family (*11*), *gl*FBPA belongs to class II. Our goal is to define the determinants of catalysis and substrate specificity of *gl*FBPA and to discover inhibitors that serve as leads for drug development. In previous work, we showed that *gl*FBPA does not cleave TBP, which is a competitive inhibitor of the enzyme ($K_i = 1\ \mu M$), despite the higher level of sequence identity of *gl*FBPA with *ec*TBPA (38%) compared with *ec*FBPA (23%) (*10*). We also confirmed that replacement of a key catalytic aspartic acid residue (Asp83 in *gl*FBPA numbering) with alanine using site-directed mutagenesis eliminated enzyme activity. This information provides the framework for the current study, which compares the structure of the ligand-free enzyme with the structures of the *gl*FBPA−TBP and D83A *gl*FBPA−FBP complexes to obtain insight into substrate-induced changes in active site structure and into the mechanisms of substrate recognition and activation.

METHODS

Crystallization and Data Collection. Recombinant wild-type *gl*FBPA and the D83A and D255A *gl*FBPAs mutants were produced and purified as described previously (*10*). Electrospray ionization time-of-flight mass spectrometry was performed in the University of New Mexico facility, to show that the N-terminal methionine is removed by posttranslational modification. Crystals were grown at room temperature in hanging drops using the vapor diffusion method. Orthorombic crystals were obtained from a protein solution that was mixed with an equal volume of mother liquor containing 18−25% polyethylene glycol 3350 and 0.2 M NH_4NO_3. Hexagonal crystals of ligand-free enzyme were obtained from mother liquor containing 0.2 M $MgSO_4$. The hexagonal crystals diffracted X-rays to a resolution of 2.9 Å. Orthorhombic crystals of the wild-type protein in complex with TBP were obtained from protein solutions that were incubated on ice for 20 min with 10 mM TBP prior to crystallization. The crystals diffracted X-rays to a resolution of 1.8 Å. Orthorhombic crystals of D83A *gl*FBPA in complex with FBP were obtained from protein solutions that were incubated on ice for 20 min with 20 mM FBP prior to crystallization. The crystals diffracted X-rays to a resolution of 2.0 Å. All crystals required a period of 2−5 weeks to appear. For data collection, the crystals were transferred to solutions containing mother liquor and 20% glycerol and flash-cooled in liquid nitrogen.

Diffraction data were acquired at 100 K using an RAXIS IV^{++} image plate detector mounted on a Rigaku MicroMax 007 rotating anode X-ray generator (Rigaku MSC Inc.). Data processing was carried out using CrystalClear, version 1.3.6 (Rigaku MSC Inc.). The statistics of data collection are provided in Table 1.

Structure Determination and Refinement. The crystal structures were determined by Molecular Replacement with the computer program Phaser (*12*), using the high-resolution orthorhombic (space group $C222_1$) FBPA−PGH structure as the search model (PDB entry 2ISW). When difference Fourier maps indicated alternative tracing, new segments were modeled manually using O (*13*). Structure refinement was carried out using CNS (*14*). For apo FBPA, refined at 2.9 Å resolution, only positional and group *B*-factor refinement with a bulk solvent correction was performed, whereas individual *B*-factors were refined for the FBPA complexes

Table 1: X-ray Data Collection and Refinement Statistics

	wild type−TBP	D83A−FBP	wild type
	Data Collection		
space group	$P2_12_12_1$	$P2_12_12_1$	$P6_1$
cell dimensions			
a, *b*, *c* (Å)	56.3, 67.6, 171.7	56.5, 67.2, 172.2	62.9, 62.9, 318.6
resolution range (Å)	20−1.8	20−2.0	10−2.9
no. of observations	338737	126831	25089
no. of unique reflections	57852	41123	13288
completeness (%)[a]	93.9 (62.9)	90.6 (50.4)	86.6 (98.7)
$I/\sigma(I)$[a]	15.1 (1.9)	10.9 (2.5)	6.0 (2.5)
R_{merge}[a,b]	0.066 (0.342)	0.051 (0.257)	0.114 (0.250)
	Refinement Statistics		
no. of reflections	57851	41081	12210
no. of residues	637	635	592
no. of water molecules	578	569	0
no. of Zn^{2+} ions	2	4	2
R_{cryst}/R_{free}[c]	0.199/0.240	0.198/0.254	0.220/0.286
rms deviation			
bonds (Å)	0.018	0.014	0.016
angles (deg)	1.7	1.7	1.7

[a] The values in parentheses are for the highest-resolution shell. [b] $R_{merge} = \sum_{hkl}(\sum_j|I_j - I|/\sum_j|I_j|)$, for equivalent reflections. [c] $R_{cryst} = \sum_{hkl}||F_o| - |F_c||/\sum_{hkl}|F_o|$, where F_o and F_c are the observed and calculated structure factors, respectively. R_{free} is computed for 5% of reflections that were randomly selected and omitted from the refinement.

determined at higher resolution. The two molecules in the asymmetric unit were refined independently. Water molecules were added to the model on the basis of the $F_o - F_c$ difference Fourier electron density map (where F_o and F_c are the observed and calculated structure factors, respectively), using peaks with a density of $\geq 3\sigma$ as the acceptance criterion. The final stages of refinement of the apo FBPA structure were performed with REFMAC (*15*). PROCHECK was used for analysis of geometry (*16*), QUANTA for molecular modeling and structural alignment (Molecular Simulations Inc.), and PYMOL for depiction of the structures (*17*).

Steady-State Kinetic Constant Determination of D255A glFBPA. Initial velocities were measured at 25 °C using 1 mL reaction solutions containing *gl*FBPA [0.5 μM for monitoring FBP (Sigma) cleavage and 30 μM for monitoring TBP (a gift from W.-D. Fessner of TU Darmstadt, Darmstadt, Germany) cleavage], 200 μM NADH (Sigma), 5 units of triosephosphate isomerase (Sigma), 2 units of glycerol-3-phosphate dehydrogenase (Sigma), and varying concentrations of FBP or TBP ($0.5K_m$to $10K_m$) in 50 mM K^+HEPES (pH 7.5). The absorbance of the reaction solution was monitored at 340 nm ($\varepsilon = 6.2$ mM^{-1} cm^{-1}).

To determine the kinetic constants, the initial velocity data were fitted to eq 1 with KinetAsystI (IntelliKinetics).

$$V_0 = V_{max}[S]/(K_m + [S]) \quad (1)$$

where [S] is the substrate concentration, V_0 is the initial velocity, V_{max} is the maximum velocity, and K_m is the Michaelis−Menten constant for the substrate. The k_{cat} value was calculated from V_{max} and the enzyme concentration [E] [determined employing the Bradford method (*18*)] using the equation $k_{cat} = V_{max}/[E]$.

Sequence Search and Alignment. Sequence analysis was carried out against microbial genomes (containing 940 bacterial and 48 archeal genomes in NCBI) using BLAST (*19*) with an inclusion *E* value threshold of 1×10^{-5}. Sequence relatives of *gl*FBPA were aligned using MUSCLE (version 3.6) with its default parameters (*20*). Amino acid multiple-sequence alignment displayed as logos diagrams was generated using WebLogo (http://weblogo.berkeley.edu/logo.cgi) (*21*).

RESULTS AND DISCUSSION

Overall Structure of glFBPA. The structure refinement statistics are summarized in Table 1, and electron density maps in the vicinity of the active site are shown in Figure 2. All structures of *gl*FBPA contain two tightly packed protein molecules in the asymmetric unit corresponding to the biological unit. Each subunit (denoted A and B) folds into an $(\alpha/\beta)_8$ barrel as seen in structures of the *gl*FBPA−PGH complex and in the structures of other bacterial class II aldolases (*3*−*6, 22*).

(i) Apo glFBPA. The ligand-free *gl*FBPA crystals were fragile and very sensitive to manipulation. They diffracted to a resolution of only 2.9 Å and exhibited high mosaic spread (2.5°). Therefore, no water molecules were assigned. The model contains 592 amino acid residues, four sulfate anions, and two zinc cations. Superposition of the two *gl*FBPA subunits yields a root-mean-square deviation (rmsd) in α-carbon positions of 0.5 Å. No electron density is associated with the following surface residues: 138−152, 175−190, 323, and 324 in molecule A and 138−152, 187−190, 323, and 324 in molecule B. These residues were omitted from the final model. The active site of each subunit is occupied by one Zn^{2+} and two sulfate ions that are positioned 9 Å apart. The sulfate ions originated from the crystallization solution (0.2 M $MgSO_4$), and they occupy the FBP or TBP phosphoryl sites. A similar result was obtained for the positions of two sulfate ions bound in the active site of apo FBPA from *Thermus aquaticus*, which was crystallized from a solution containing ammonium sulfate (*22*). Because the positions and interactions of the sulfate ions in the ligand-free *gl*FBPA structure overlap with those of the phosphoryl groups of the FBP and TBP ligands, the detailed description of the interactions will be discussed in the section describing these ligands.

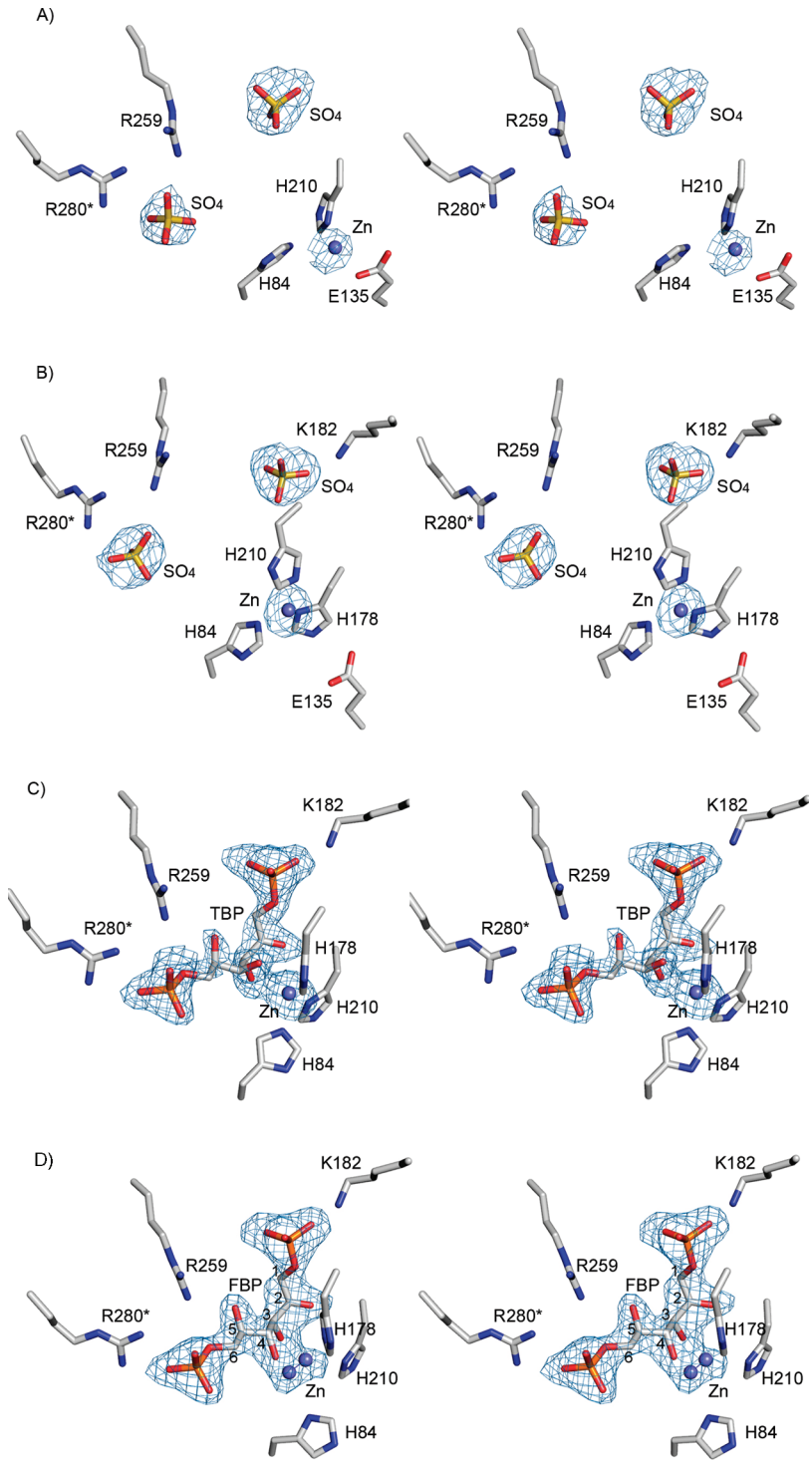

FIGURE 2: Stereoscopic view of the electron density map in the vicinity of the active site. Difference Fourier electron density maps with the coefficients $F_o - F_c$ and calculated phases generated via omission of the ligands and zinc cofactors from the models. The maps are countered at the 3σ level. (A and B) The apo structure contains sulfate ions, and each subunit of the dimer exhibits a different Zn^{2+} environment. Data resolution of 2.9 Å. (C) Bound TBP. Data resolution of 1.8 Å. (D) Bound FBP. Data resolution of 2.0 Å.

Each subunit contains a Zn^{2+} cofactor (Figure 2A,B). In molecule A, Zn^{2+} coordinates the Glu135 carboxyl group and His210 and is located 3.2 Å from His84 (too far for direct coordination) (Table 2). The loop comprising residues 176−187 and containing the active site His178 is disordered. In molecule B, Zn^{2+} coordinates all three histidine residues, His84, His210, and His178.

(ii) FBPA−TBP Complex. The model includes 637 amino acid residues and 578 water molecules. Each active site is occupied by a TBP ligand (Figure 2C). Pairwise superposition of two monomers results in a rmsd between α-carbon positions of 0.3 Å. No electron density is associated with surface residues 144−146 in molecule A and residues 144−147 in molecule B. These residues were omitted from the final model.

(iii) D83A FBPA−FBP Complex. The model includes 635 amino acid residues and 569 water molecules. Each active site is occupied by a FBP ligand and a Zn^{2+} ion, which binds in two mutually exclusive sites, each with half-occupancy (Figure 2D). Pairwise superposition of the two monomers

Table 2: Metal−Ligand Interactions in Class II FBPAs

structure	metal site	ligands	distance[a] (Å)	notes
apo *gl*FBPA				
molecule A	Zn1	His210 Nδ1	2.0	2.9 Å resolution structure
		His84 Nε2	(3.2)	no solvent model
		Glu135 Oε1	(3.1)	incomplete coordination geometry
		Glu135 Oε2	2.2	
molecule B	Zn2	His210 Nδ1	2.3	as above
		His84 Nε2	2.2	
		His178 Nε2	2.8	
*gl*FBPA−TBP	Zn2	His210 Nδ1	2.3	trigonal bipyramidal
		His84 Nε2	2.4	
		His178 Nε2	2.2	
		TBP C(2)O	2.9	
		TBP C(3)O	2.6	
*gl*FBPA−PGH [PDB entry 2isw (*10*)]	Zn2	His210 Nδ1	2.2	trigonal bipyramidal
		His84 Nε2	2.1	Zn^{2+} is coplanar with the PGH's O-C(2)-N(3)-O group
		His178 Nε2	2.3	
		PGH C(2)O	2.5	
		PGH N(3)O	2.6	
D83A *gl*FBPA−FBP	Zn2A	His210 Nδ1	2.9	mutually exclusive with Zn2B, highly distorted pentagonal coordination
		His84 Nε2	(3.4)	
		His178 Nε2	(3.1)	
		FBP C(3)O	2.2	
		FBP C(4)O	2.1	
	Zn2B	His210 Nδ1	(3.5)	mutually exclusive with Zn2A; when Asp83 is modeled (Figure 5),
		His84 Nε2	(3.0)	forms highly distorted pentagonal coordination that includes Asp83;
		FBP C(3)O	2.1	Zn^{2+} is coplanar with the O-C(3)-C(4)-O group
		FBP C(4)O	2.2	
apo *ec*FBPA				
PDB entry 1zen (*4*)	Zn1	His264 Nδ1	2.4	described as distorted tetrahedral
		His110 Nε2	2.6	
		His226 Nε2	2.5	
		Glu174 Oε1	2.5	
		Glu174 Oε2	2.8	
	Zn3	His264 Nδ1	2.6	described as distorted tetrahedral
		Lys284 Nζ	2.7	
		Asp109 Oδ1	2.5	
		Glu172 Oε1	2.9	
		Glu172 Oε2	2.5	
PDB entry 1dos (*3*)	Zn1	His264 Nδ1	2.1	mutually exclusive with Zn2, tetrahedral
		His110 Nε2	2.1	
		His226 Nε2	2.1	
		Glu174 Oε2	2.3	
	Zn2	His264 Nδ1	2.3	mutually exclusive with Zn1, tetrahedral
		His110 Nε2	2.1	
		Wat1 O	2.4	
		Wat2 O	2.3	
*ec*FBPA−PGH [PDB entry 1b57 (*5*)]	Zn2	His264 Nδ1	1.9	trigonal bipyramidal
		His110 Nε2	2.1	Zn^{2+} is coplanar with the PGH O-C(2)-N(3)-O group
		His226 Nε2	1.9	
		PGH C(2)O	2.2	
		PGH N(3)O	2.3	
	Zn4	Glu174 Oε2	2.0	tetragonal
		Glu181 Oε2	1.9	
		Asp144 Oδ2	2.0	
		Wat O	2.1	

[a] The values in parentheses indicate distances that are too large for optimal Zn−ligand coordination; nevertheless, these residues are oriented toward the Zn.

results in a rmsd between α-carbon positions of 0.3 Å. No electron density is associated with residues 144−147 in molecule A and residues 144−148 in molecule B. These residues were omitted from the final model.

Structural Changes upon Ligand Binding. Pairwise superposition of both molecules of apo and ligand-bound *gl*FBPA shows local changes in loop regions (Figure 3). These loops are located remotely from crystal contacts, and thus, the differences are attributed solely to ligand binding. The most striking response to both FBP and TBP binding is the ordering of the loops spanning residues 135−155 and residues 174−194, which are largely disordered in the ligand-free FBPA structure. The 174−194 loop caps the ligand C(4)−C(6) atoms; on the other hand, the 135−155 loop tucks in the 174−194 loop and four of its residues that do not contact the 174−194 loop remain disordered (144−147). When ligand binds, Lys182 and His178 located on the 174−194 loop form key interactions with FBP or TBP and the Zn^{2+} (Figures 2 and 4). A third loop, encompassing residues 227−237, undergoes substantial rearrangement, with the Ala233 and Val234 Cα atom positions in the middle of the loop shifting by 2.7 Å from their positions in the ligand-free structure to accommodate the 174−194 loop (Figure 3).

Substrate Binding Site. To obtain detailed molecular insights into catalysis and substrate recognition, we deter-

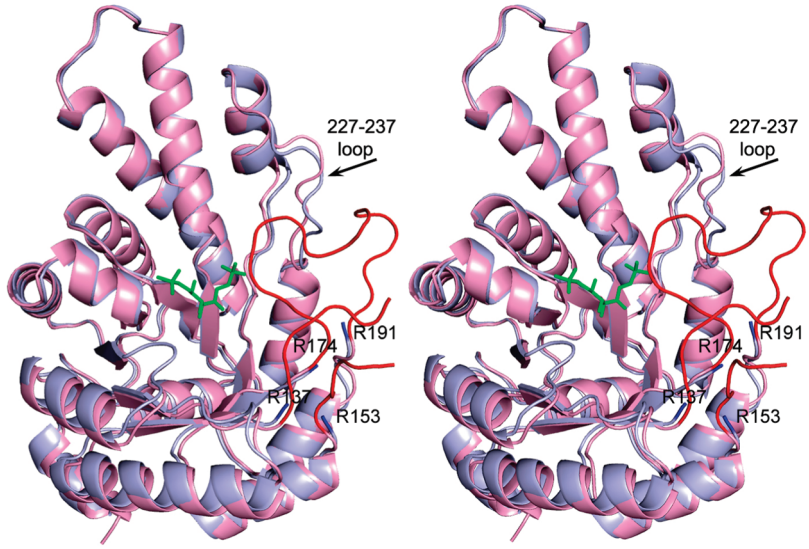

FIGURE 3: Stereoscopic representation of *gl*FBPA in the unbound and ligand-bound states. The superposed molecules are depicted in blue (unbound) and pink (bound state) where the trace of the polypeptide chain is similar in both structures. The major differences occur in two loop regions. The terminal fragments of the two disordered loops of the apo *gl*FBPA structure are highlighted in blue, and the same loops of the *gl*FBPA−FBP structure are highlighted in red. The FBP is depicted as a green stick model.

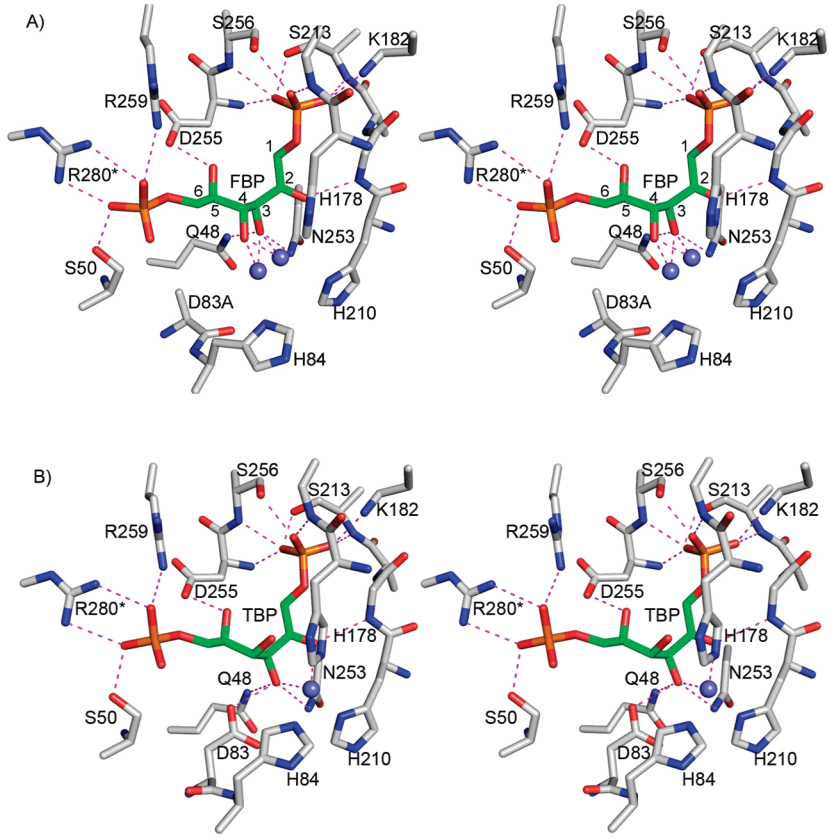

FIGURE 4: Binding of FBP (A) and TBP (B) to *gl*FBPA. Stereoscopic view of the environment around the active site. Atomic colors are as follows: oxygen, red; nitrogen, blue; carbon (protein), gray; carbon (ligand), green; phosphorus, orange; and zinc, steel blue. Key electrostatic interactions of the ligands are shown as dashed lines.

mined the crystal structure of wild-type *gl*FBPA in complex with the FBP C(4) hydroxyl epimer, TBP, which is a competitive inhibitor of the enzyme, and that of the D83A *gl*FBPA mutant in complex with the substrate FBP (Figure 4). The two crystals are isomorphous, and the D83A mutation does not alter the overall fold as evidenced by the superposition of the two structures that yields an rmsd between Cα traces of 0.3 Å. It is clear from the electron density maps that both ligands bind in the acyclic keto form of their respective hexoses (Figure 2C,D), although it has been reported that in solution FBP exists mainly (ca. 98%) in the cyclic hemiketol form (*23*). Indeed, the active site is a rather narrow crevice designed to accommodate an acyclic substrate. The K_i of 1 μM of the tagatose inhibitor, when adjusted to reflect the population of the acyclic form, defines a remarkably low K_d of 20 nM.

As seen in the *gl*FBPA−FBP complex, the two ends of the substrate are pinned into place via interactions of

electropositive residues with the C(1) and C(6) phosphate groups (Figure 4A). The conformation of the substrate at the reaction center [viz. the C(3)−C(4) bond] is further defined through formation of a hydrogen bond between the Gly211 NH and Asp255 carboxylate group with the C(2)═O and C(5)OH groups, respectively. Finally, the C(3)OH group is anchored by its interaction with Gln48 and Asn253 side chains and the Zn^{2+}, whereas the C(4)OH group is anchored by its interactions with the Zn^{2+}. As discussed later, modeling that restores Asp83 instead of the alanine mutant shows that the C(4)OH group also interacts with the Asp83 carboxylate group (Figure 5).

In the following discussion, the *gl*FBPA active site is divided into three subsites: the DHAP binding site, the G3P binding site, and the Zn^{2+} binding site.

(i) DHAP Site. The interactions of the enzyme with the FBP C(1)−C(3) moiety deviate from the interactions observed with the PGH inhibitor (*10*), whereas the interactions of the enzyme with the TBP C(1)−C(3) moiety do not. The FBP/TBP C(1)−C(3) moiety binds in a deep polar cavity with the C(1) dianionic phosphate group stationed in a site enriched with positive dipoles of backbone amide groups (Gly179, Ser213, Asp255, and Ser256) (Figure 4). In addition, the C(1) phosphate interacts with the amino group of Lys182 on the 174−194 flexible loop and with the hydroxyl groups of Ser213 and Ser256. Unlike the PGH C(2)O group, which forms a hydrogen bond with the Gly211 backbone amide group concomitantly with coordination to the Zn^{2+}, the FBP C(2)═O group interacts only with the backbone amide group of Gly211. In contrast to FBP, the C(2)═O group of the TBP exhibits the same two interactions as those of the PGH. The C(3)OH group of FBP and TBP and the N-OH group of PGH are all coordinated to the Zn^{2+}, and they also form hydrogen bonds with the side chain amide groups of Asn253 and Gln48.

(ii) G3P Site. The C(6) phosphate groups of both FBP and TBP interact with the Arg259 guanidinium group and that of Arg280 of the partner subunit (Arg331 in *ec*FBPA) (Figure 4). The latter interaction is consistent with previous site-directed mutagenesis results: Arg331 is essential for the C(6) phosphate group binding as evidenced by the R331A and R331Q *ec*FBPA mutants for which the K_m values for FBP are dramatically increased whereas the K_m values for DHAP are unchanged (*24*). Both Arg259 and Arg280 of *gl*FBPA participate in an exquisite charge network that anchors them for optimal interaction with the ligand. Asp255 and Asp278 of the partner subunit interact with Arg259, and in turn Asp278 interacts with Arg280. Ser50, conserved in class II FBPAs (Ser61 in *ec*FBPA), forms a hydrogen bond with the C(6) phosphate group. Again, site-directed mutagenesis experiments with the *ec*FBPA demonstrated the importance of this interaction. First, the catalytic efficiency of the S61A FBPA is significantly lower (increased K_m and decreased k_{cat}) than that of the wild-type enzyme, and second, whereas the wild-type enzyme exhibited G3P product inhibition, the S61A mutant did not (*8*).

(iii) Shifting Zn^{2+} Site. The electron density maps of all *gl*FBPA structures revealed a metal bound in the active site. Previously, we used tunable synchrotron X-rays to show a peak at 9674.2 eV corresponding to the absorption edge of Zn (*10*). No zinc was added during protein purification and crystallization, which indicates a high affinity of the enzyme for the Zn^{2+}. The same protein purification protocol was employed in our studies. Also, the metal−ligand coordination distances are ∼2.0−2.3 Å, and the metal coordinates histidine side chains, which is typical of Zn^{2+} (Table 2). Taken together, the evidence supports Zn^{2+} as the intrinsic metal bound in the active site.

One of the striking structural features of the class II Zn^{2+}-dependent FBPAs is the promiscuity of the Zn^{2+} sites, coordination geometry, and ligands. Analysis of zinc geometry in protein structures refined at a resolution higher than 2 Å showed that the Zn^{2+} coordination distance to oxygen atoms is 2.3 ± 0.3 Å and to nitrogen atoms 2.1 ± 0.2 Å (*25*). As can be seen by viewing the data in Table 2, the Zn^{2+} coordination distances in *gl*FBPA are sometimes outside this range. We bracket potential ligands, which are located more than 3 Å from the metal, to indicate weak interactions but nevertheless included them to contrast the different structures.

Previously, three Zn^{2+}-containing structures of *ec*FBPA, two ligand-free structures and one *ec*FBPA−PGH complex, were described (*3*−*5*). One of the ligand-free structures (PDB entry 1zen) contains two Zn^{2+} ions, each exhibiting a coordination geometry described as distorted tetrahedral (*4*). We assigned these sites as Zn1 and Zn3 (Table 2). Another independently determined apo structure [PDB entry 1dos (*3*)] revealed two mutually exclusive Zn^{2+} sites with approximately one-half occupancy each. One site, corresponding to the Zn1 site that was described by Cooper and colleagues (*4*), and the second site, which we assign as Zn2 (Table 2), are not present in PDB entry 1zen. The structure of the *ec*FBPA−PGH complex (*5*) exhibits two Zn^{2+} binding sites in each subunit [Zn2 and Zn4 (Table 2)]. The authors proposed that Zn2 plays a catalytic role because it coordinates to the PGH O-C(2)-N(3)-O moiety. The zinc at the Zn4 site on the other hand was suggested to play a structural role. The new *gl*FBPA structures reported here reveal further diversity in Zn^{2+} binding.

Difference Fourier electron density maps (Figure 2A,B) show bound Zn^{2+} in both molecules of the crystal asymmetric unit of apo *gl*FBPA, corresponding to Zn1 (in molecule A) and Zn2 (in molecule B). In molecule A, Zn^{2+} coordinates the side chains of His210 and Glu135 (Figure 2A). His84 is oriented toward the metal, but the distance is too great for direct coordination (3.2 Å). In molecule B, Zn^{2+} coordinates three histidine residues His84, His210, and His178 (Figure 2B). Because of the limited resolution of the diffraction data (2.9 Å), no water molecules could be assigned in the electron density map, and therefore, water ligands that might complete the Zn^{2+} coordination sphere elude detection.

In the *gl*FBPA−TBP complex, the Zn^{2+} is bound at the Zn2 site. The Zn^{2+} exhibits a trigonal bipyramidal coordination geometry that is similar but not identical to that seen in both *gl*FBPA and *ec*FBPA in complex with PGH, and it is located in the Zn2 site. Three Zn^{2+} ligands are provided by histidine residues: the N^{ε} atoms of His84 and His178 and the N^{δ} atom of His210 (Figure 2C). The TBP contributes C(2)O and C(3)O ligands, analogous to the C(2)O and N(3)O groups, respectively, of the PGH ligand. However, the distances from the TBP C(2)O and C(3)O groups to the zinc (2.9 and 2.6 Å, respectively) are somewhat longer than the mean value reported by Wodak and colleagues (*25*). The elongated coordination bonds serve to avoid a clash between

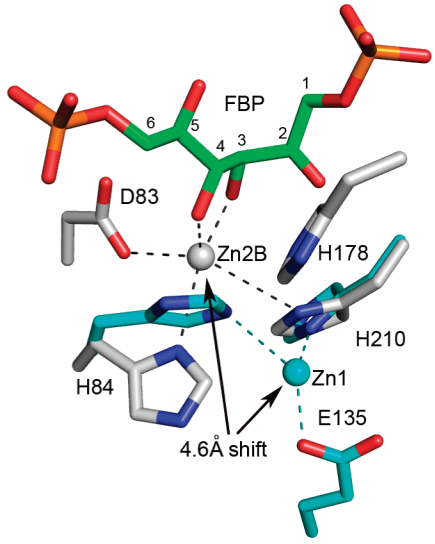

FIGURE 5: Local active site conformational transition associated with FBP binding to *gl*FBPA (with a model of Asp83 based on other wild-type *gl*FBPA structures). The Zn^{2+} position shifts by 4.6 Å toward the catalytic Asp83, which changes its coordination so that in the substrate cleavage mode (Zn2B) the Asp83 is coordinated to Zn^{2+}. The Zn^{2+} and carbon atoms of the apoenzyme are colored cyan. Other atomic colors are the same as in Figure 4. Note that His178 is disordered in the apo structure.

the TBP C(4) hydroxyl and the imidazole group of His178 (Figure 4). Unlike the O-C(2)-N(3)-O group of the PGH ligand, the O-C(2)-C(3)-O atoms of the TBP ligands are not coplanar with the Zn^{2+}.

For the D83A *gl*FBPA−FBP complex, the difference Fourier map (Figure 2D) shows electron density for both molecules in the asymmetric unit, consistent with two mutually exclusive Zn^{2+} ions, 1.4 Å apart and with one-half occupancy each (termed Zn2A and Zn2B in Table 2). Observations of mutually exclusive metal sites in FBPA have been reported. Specifically, dual metal binding occurs in one of the four protein molecules in the asymmetric unit of the class II *T. aquaticus* FBPA apo structure, where two mutually exclusive cobalt ions (2.5 Å apart) were modeled (*22*). In addition, in the *ec*FBPA apo structure (PDB entry 1dos), there are also two mutually exclusive Zn^{2+} ion binding sites, 3.2 Å apart; each of these sites is associated with alternate conformations of the two coordinated histidine residues, His10 and His264 (Table 2). Both alternate zinc sites of the D83A *gl*FBPA−FBP complex exhibit highly perturbed pentagonal geometry with long distances to the potential histidine ligands (in contrast to the short distances to the histidine residues in the PGH and TBP complexes) and typical oxygen coordination distances (2.1−2.2 Å) to the FBP C(3) and C(4) hydroxyl groups (Table 2). The location of the Zn2A site is close to that of Zn2 in the PGH- or TBP-inhibited enzyme (1.0 or 0.9 Å apart, respectively). The Zn2B site is 2.3 Å from the Zn2 site and is unique because it is the only metal site observed in the collection of FBPA structures that allows coordination of the Asp83 [missing in the inactive D83A mutant, but modeling the Asp83 based on all other *gl*FBPA structures suggests an ~2.2 Å coordination distance (Figure 5)]. Notably, the O-C(3)-C(4)-O group of the FBP ligand and the Zn2B are coplanar. The Ala83-His84 peptide bond in the D83A *gl*FBPA−FBP complex adopts an α-helical conformation ($\varphi = -61°$, and $\psi = -36°$), whereas it adopts a β-conformation in the *gl*FBPA−TBP complex ($\varphi = -88°$, and $\psi = 138°$). Inspection of the two structures suggests that the conformational change may be attributed to the effect of the mutation; the Asp83 side chain orientation as seen in all wild-type FBPA structures ($\chi_1 = 180°$) results in steric clash with an ensuing helical peptide carbonyl group as seen in the D83A mutant enzyme, and the backbone CO of the mutated enzyme forms a hydrogen bond with an internal water molecule that is otherwise provided by Asp83 in the wild-type enzyme. In our discussion of the role of Zn2B in catalysis, which follows, we assume that the wild-type FBPA Asp83-His84 peptide maintains the β-conformation.

Catalytic Mechanism: Implications of the New Structures. We suggest for consideration and future experimental exploration a modification to the class II aldolase catalytic mechanism proposed earlier on the basis of PGH-bound *ec*FBPA and *ec*TBPA structures, which incorporates the insights provided by the liganded *gl*FBPA structures (Figure 6). On the basis of the structures of *ec*FBPA, Hunter, Berry, and colleagues proposed that Asp109 (Asp83 in *gl*FBPA) abstracts a proton from the FBP C(4)OH group in the C(3)−C(4) bond cleavage step, which leads to the ene-diolate intermediate, and that Glu182 (Glu143 in *gl*FBPA) protonates the ene-diolate at C(3) in the ensuing step (*5*, *9*). The structures of *gl*FBPA in complex with either FBP or TBP reveal for the first time the identities of substrate binding residues and the catalytic residues "in total". Thus, in the presence of FBP and TBP, the flexible 138−152 loop adopts a conformation that places the Glu143 carboxylate group 23 Å from C(3) of FBP or TBP. In the complex with the PGH (the analogue of the ene-diolate intermediate), residues 140−149 are disordered and Glu143 is undefined. Nevertheless, it is clear from the rest of the structure that the Glu143 carboxylic group is unlikely to reach the C(3) position, and therefore, its carboxylate group may not play the role of general acid. This conclusion is also consistent with the reported finding that the E182A *ec*FBPA mutant exhibits an only 37-fold reduction in catalytic efficiency (*9*). The *gl*FBPA−FBP structure indicates that when Asp83 is modeled into position (by analogy to its position in the PGH- or TBP-bound enzymes), the side chain is 3.3 Å from the C(4) hydroxyl and 3.4 Å from C(3) of FBP. We propose a stepwise mechanism in which Asp83 serves as both a general base and a general acid because it is poised appropriately for accepting the proton from the C(4)OH group and, as the conjugate acid, delivering it to C(3) of the putative ene-diolate intermediate.

The second finding from the *gl*FBPA−FBP structure, and in particular the Zn2B site, is that upon migration to this site the Zn^{2+} is positioned to orient and polarize the FBP C(4)OH group, and simultaneously orient the side chain of Asp83, for proton transfer from the C(4)OH group to the Asp83 carboxylate group. Thus, the Zn^{2+} is an active participant in catalysis of C(4)OH deprotonation. The Zn^{2+} is also positioned to assist in the polarization of the FBP C(4)−C(3) bond. Specifically, coordination of Zn^{2+} to the C(3)OH group coupled with the hydrogen bonds donated by Gln48 and Asn253 side chains serves to augment the interaction of the Gly211 backbone amide with the C(2)═O group in stabilization of the transition state leading to the ene-diolate intermediate depicted in Figure 6.

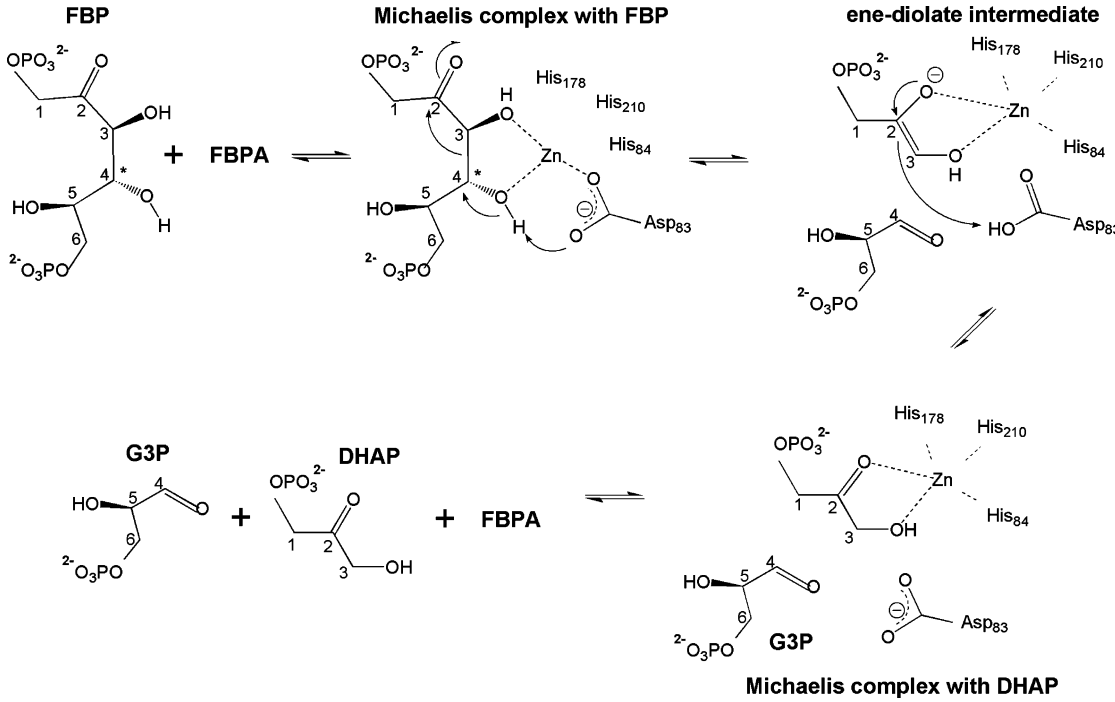

FIGURE 6: Proposed catalytic mechanism of class II FBPA. The FBP C(4) position, the chirality of which distinguishes FBP from TBP, is indicated with an asterisk. Carbon numbering from 1 to 6 is maintained also after bond cleavage for the sake of clarity.

The most intriguing feature of the Zn^{2+} cofactor is that it can migrate 4.6 Å from the Zn1 site to the Zn2B site, and that its coordination changes along the way (Figure 5). The plasticity of Zn^{2+} coordination may be an important factor in catalysis. Ideally, coordination of Zn^{2+} to the FBP C(3)O and C(4)O groups would be maximal at the first transition state and not at the ground state. The in-plane and out-of-plane Zn^{2+} coordination revealed by the three structures suggests mobility of the Zn^{2+} that might allow it to maximize coordination with the C(3)O coordination as C(4) changes hybridization state in formation of the first transition state. Furthermore, the reduction in the strength of the coordination bond of Zn^{2+} with Asp83 upon protonation might drive the reorganization of the Zn^{2+} inner coordination sphere, and the movement of Zn^{2+} to coordinate with the C(2)O and C(3)O groups of the ene-diolate intermediate may guide the Asp83 conjugate acid for proton delivery. At this stage, C(3) of the ene-diolate becomes the obvious candidate for accepting the proton. In future work, the model of catalysis inferred from the structures will be tested by site-directed mutagenesis coupled with kinetic and structural analysis of the mutants.

Substrate Specificity. Intriguingly, whereas both the amino acid sequence and crystal structure of *gl*FBPA are more similar to those of *ec*TBPA than to those of *ec*FBPA (38 and 23% identical in sequence, respectively), the kinetic characterization showed unequivocally that the true substrate is FBP (*10*). Moreover, in contrast to *ec*FBPA, *gl*FBPA recognizes TBP as a tight binding inhibitor rather than as a substrate (*10*). We have now shown that as with the substrate FBP, TBP binds to the *gl*FBPA active site in the acyclic ketone form; however, because of the difference in the stereochemistry at C(4), the C(4)OH group of the TBP ligand is not coordinated by the Zn^{2+}, nor is it positioned for proton abstraction by the putative general base Asp83 (Figure 4). On the other hand, all other binding interactions remain unchanged, thus accounting for tight TBP binding without catalytic turnover. For the C(4)OH group of the TBP ligand to assume the position of the C(4)OH group of the FBP ligand, rotation about the C(3)−C(4) bond must occur. Such rotation is expected to disrupt the favorable interaction between the C(5)OH group and Asp255 and possibly the interaction of the C(6) phosphate group with Arg259, Arg280* (of the partner subunit), and Ser50 (Figure 4).

The *gl*FBPA Asp83 counterpart in *ec*TBPA, Asp82, occupies the same position in the *ec*TBPA active site that Asp83 does in the *gl*FBPA active site (*10*) and Asp109 in *ec*FBPA (*6*). Thus, we anticipate that during catalysis, the respective C(4)OH groups are colocated, whereas the respective C(5)OH and C(6) phosphate groups are not. Perhaps it is no coincidence that *ec*TBPA does not conserve an aspartate at the site defined by Asp255 of *gl*FBPA (Asp288 of *ec*FBPA and Ala232 of *ec*TBPA) as the C(5)OH group will not be properly positioned for formation of a hydrogen bond with this residue [i.e., assuming that the C(4)OH group must be oriented to form the same interactions with the catalytic aspartate and the Zn^{2+}]. To test this hypothesis, we replaced Asp255 of the *gl*FBPA with Ala so that its interaction with the TBP C(5)OH group is eliminated, which in turn might allow a TBP C(4)−C(3) bond rotation. D255A *gl*FBPA was expressed, purified, and characterized using steady-state kinetics (Table 3), showing that the mutant enzyme cleaves TBP (albeit with low efficacy; $k_{cat}/K_m = 80\ M^{-1}\ s^{-1}$) while losing 50-fold catalytic efficacy toward FBP. Interestingly, the K_m values of the mutant enzyme toward FBP and TBP are similar, and they are 10−20 times higher than the FBP K_m of the wild-type enzyme. Earlier, Zgiby et al. reported that the D288A *ec*FBPA mutant did not display enhanced TBPA activity (*8*). Because the *gl*FBPA structure resembles that of the *ec*TBPA more closely than that of *ec*FBPA, it may be more tolerant of the Ala for Asp replacement.

Potential Sequence Signatures of FBP versus TBP Selectivity. The high level of sequence identity (38%) between *gl*FBPA and *ec*TBPA may account for the ability to introduce

Table 3: Steady-State Kinetic Parameters for Wild-Type and D255A Mutant *gl*FBPA

substrate	parameter	wild type	D255A
FBP	k_{cat} (s^{-1})	3.55 ± 0.05	0.63 ± 0.03
	K_m (μM)	1.7 ± 0.1	16 ± 2
	k_{cat}/K_m (M^{-1} s^{-1})	2 × 10^6	4 × 10^4
TBP	k_{cat} (s^{-1})	−[a]	0.003 ± 0.0002[a]
	K_m (μM)	−	37 ± 7
	k_{cat}/K_m (M^{-1} s^{-1})	−	80

[a] The limit of detection of TBPA activity is 1 × 10^{-5} s^{-1}. The observed k_{cat} for the D255A mutant is 2 orders of magnitude higher.

the new activity by a single-residue mutation. While the D255A mutation introduces new activity toward TBP, the single replacement does not fully switch stereospecificity. This is not surprising because the 38% level of sequence identity between *gl*FBPA and *ec*TBPA means that 62% of the residues are different, providing ample opportunity for additional built-in specificity determinants. For the purpose of identifying other important substrate discrimination determinants, we have analyzed the FBPA/TBPA sequence family using BLAST (*19*). The sequence search of the microbial genomes database resulted in 513 hits. Of these, 301 sequences contained an aspartic acid residue in the position corresponding to Asp255 of *gl*FBPA, and 60 sequences contained alanine at this position. The remaining sequences contained residues other than aspartate or alanine at position 255 and were excluded from further analysis. The annotations of most remaining sequences were consistent with the FBPA and TBPA division; however, some sequences were annotated as FBPA/TBPA enzymes. To ensure "clean" grouping, the sequences with dual activity annotation were removed from the analysis even though the basis for the annotation is not provided in the sequence database, leaving 289 sequences in the FBPA group and 51 sequences in the TBPA group.

Having produced two subfamilies based on the Asp or Ala at position 255, we then examined residue preferences in other sequence positions. Although the key residues involved in substrate interactions tend to be conserved in both groups, there are several clusters in the alignment that may comprise the FBP/TBP specificity signature, especially in residues located in the first shell surrounding the ligand (defined by a distance between any ligand atom to a first-shell residue that is shorter than 4 Å) and the second-shell residues (defined by distances between any residue and a first-shell residue that are shorter than 4 Å) (Figure 7).

The first stereospecificity signature sequence comprises residues 48−53 (*gl*FBPA numbering). In this region, Gln48 and Ser50 of the FBPA group (Figure 7A) are first-shell residues. In the *gl*FBPA structures, the NH_2 group of Gln48 interacts with the C(3)OH group of the FBP and TBP (3.2−3.5 Å) (Figure 4). Replacement with an alanine (the highest-frequency residue in the TBPA group) makes the environment less crowded and provides more flexibility that may help with TBP accommodation in a productive binding mode. Ser50 interacts with the C(6) phosphoryl group of both ligands (Figure 4). The threonine in this position is characteristic of the TBPA subfamily, and it forms a hydrogen bond with another TBPA conserved threonine residue in position 53, a second-shell residue (Ala in *gl*FBPA). The Pro at position 51, also a second-shell residue,

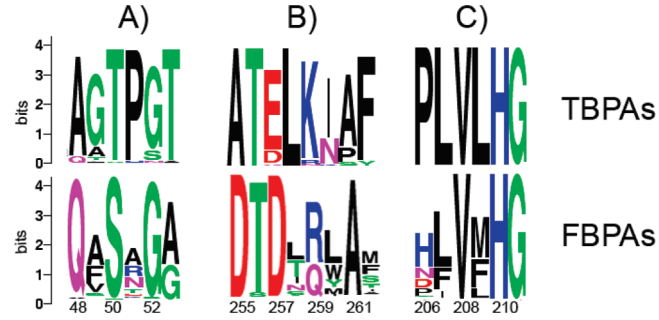

FIGURE 7: Sequence logos (*27*) of multiple-sequence alignment for three regions of the FBPA and TBPA subfamilies. The overall height of the stack indicates the level of sequence conservation at each position, and the height of symbols within the stack indicates the relative frequency of the particular amino acid at the position. The *gl*FBPA numbering was used, and every other amino acid residue is numbered.

is a hallmark of the "TBPA" subgroup. This residue, together with the replacement of Arg259 [a C(6) phosphoryl interacting residue] with a Lys in the TBPA subfamily (Figure 7B), may modify the phosphate binding site slightly in a manner more suitable for productive accommodation of TBP. Moreover, Arg259 forms an ion pair with Asp255. The alternative Lys-Ala pair, as found in the TBPA subfamily (Figure 7B), leads to a less crowded phosphoryl environment that may facilitate the adjustment of the TBP in the active site.

Another interesting cluster of residues is found around His210 (Figure 7C), a Zn^{2+}-interacting residue (Figure 4). Four residues preceding this histidine (PLVL) are invariant in the TBPA subfamily, whereas only a valine at position 208 is conserved in the "FBPA" sequences. This segment is outside the first and second shells and perhaps contributes to stereoselectivity by fine-tuning the positioning of the Zn^{2+} ion and its coordination properties.

In an earlier attempt to understand the substrate specificity of class II FBP/TBP aldolases, Zgiby et al. (*8*) identified nine residues of the *ec*FBPA as having a potential impact on substrate discrimination and mutated them into the corresponding residues of *ec*TBPA. None of the mutations produced an enzyme with increased activity toward TBP, whereas many of them impaired FBPA activity. In another study, three rounds of *ec*TBPA-directed evolution by DNA shuffling produced an enzyme that exhibited a nearly 80-fold improvement in k_{cat}/K_m toward the non-natural substrate FBP (*26*). None of these evolved residues lie within the first-shell binding site envelope. Two replacements altered the enzyme stereochemistry (equivalent to *gl*FBPA positions 26 and 279). Inspection of their structural context suggests that they might have perturbed the position of the conserved arginine residue involved in C(6) phosphoryl binding [*gl*FBPA Arg280 (Figure 4)]. Two other evolved sequence positions correspond to residues invariant in both the TBPA and FBPA groups (Asp105 and Ser107 in *gl*FBPA). The side chains of these residues form a hydrogen bond network with His84, a Zn^{2+} ligand (Figure 4). Berry and co-workers suggested that the replacement of these residues with glycines changed the orientation of the substrate, leading to altered stereochemistry. Asp105 and Ser107 are second- and third-shell residues.

Taken together, our results and those from earlier studies underscore the complexity of defining substrate stereospeci-

ficity, which involve amino acid residues within the first-, second-, and higher-level shells surrounding the ligand. Moreover, there may be multiple routes for optimization of stereospecificity. Better insight into this fascinating issue will be gained from the structure of a TBPA−substrate complex.

ACKNOWLEDGMENT

We thank John Moult for insightful discussions and Patrick Mariano for critical reading of the manuscript.

REFERENCES

1. Kobes, R. D., Simpson, R. T., Vallee, R. L., and Rutter, W. J. (1969) A functional role of metal ions in a class II aldolase. *Biochemistry 8*, 585–588.
2. Rutter, W. J. (1964) Evolution of Aldolase. *Fed. Proc. 23*, 1248–1257.
3. Blom, N. S., Tetreault, S., Coulombe, R., and Sygusch, J. (1996) Novel active site in *Escherichia coli* fructose 1,6-bisphosphate aldolase. *Nat. Struct. Biol. 3*, 856–862.
4. Cooper, S. J., Leonard, G. A., McSweeney, S. M., Thompson, A. W., Naismith, J. H., Qamar, S., Plater, A., Berry, A., and Hunter, W. N. (1996) The crystal structure of a class II fructose-1,6-bisphosphate aldolase shows a novel binuclear metal-binding active site embedded in a familiar fold. *Structure 4*, 1303–1315.
5. Hall, D. R., Leonard, G. A., Reed, C. D., Watt, C. I., Berry, A., and Hunter, W. N. (1999) The crystal structure of *Escherichia coli* class II fructose-1,6-bisphosphate aldolase in complex with phosphoglycolohydroxamate reveals details of mechanism and specificity. *J. Mol. Biol. 287*, 383–394.
6. Hall, D. R., Bond, C. S., Leonard, G. A., Watt, C. I., Berry, A., and Hunter, W. N. (2002) Structure of tagatose-1,6-bisphosphate aldolase. Insight into chiral discrimination, mechanism, and specificity of class II aldolases. *J. Biol. Chem. 277*, 22018–22024.
7. Plater, A. R., Zgiby, S. M., Thomson, G. J., Qamar, S., Wharton, C. W., and Berry, A. (1999) Conserved residues in the mechanism of the *E. coli* Class II FBP-aldolase. *J. Mol. Biol. 285*, 843–855.
8. Zgiby, S. M., Thomson, G. J., Qamar, S., and Berry, A. (2000) Exploring substrate binding and discrimination in fructose 1,6-bisphosphate and tagatose 1,6-bisphosphate aldolases. *Eur. J. Biochem. 267*, 1858–1868.
9. Zgiby, S., Plater, A. R., Bates, M. A., Thomson, G. J., and Berry, A. (2002) A functional role for a flexible loop containing Glu182 in the class II fructose-1,6-bisphosphate aldolase from *Escherichia coli*. *J. Mol. Biol. 315*, 131–140.
10. Galkin, A., Kulakova, L., Melamud, E., Li, L., Wu, C., Mariano, P., Dunaway-Mariano, D., Nash, T. E., and Herzberg, O. (2007) Characterization, kinetics, and crystal structures of fructose-1,6-bisphosphate aldolase from the human parasite, *Giardia lamblia*. *J. Biol. Chem. 282*, 4859–4867.
11. Henze, K., Morrison, H. G., Sogin, M. L., and Muller, M. (1998) Sequence and phylogenetic position of a class II aldolase gene in the amitochondriate protist, *Giardia lamblia*. *Gene 222*, 163–168.
12. McCoy, A. J., Grosse-Kunstleve, R. W., Storoni, L. C., and Read, R. J. (2005) Likelihood-enhanced fast translation functions. *Acta Crystallogr. D61*, 458–464.
13. Jones, T. A. (2004) Interactive electron-density map interpretation: From INTER to O. *Acta Crystallogr. 60*, 2115–2125.
14. Brünger, A. T., Adams, P. D., Clore, G. M., DeLano, W. L., Gros, P., Grosse-Kunstleve, R. W., Jiang, J. S., Kuszewski, J., Nilges, M., Pannu, N. S., Read, R. J., Rice, L. M., Simonson, T., and Warren, G. L. (1998) Crystallography & NMR system: A new software suite for macromolecular structure determination. *Acta Crystallogr. 54*, 905–921.
15. Murshudov, G. N., Vagin, A. A., and Dodson, E. J. (1997) Refinement of macromolecular structures by the maximum-likelihood method. *Acta Crystallogr. D53*, 240–255.
16. Laskowski, R. A., and MacArthur, M. W. (1993) PROCHECK: A program to check the stereochemical quality of protein structures. *J. Appl. Crystallogr. 26*, 283–291.
17. DeLano, W. L. (2002) *The PyMOL User's Manual*, DeLano Scientific, San Carlos, CA.
18. Bradford, M. M. (1976) A rapid and sensitive method for the quantitation of microgram quantities of protein utilizing the principle of protein-dye binding. *Anal. Biochem. 72*, 248–254.
19. Altschul, S. F., Madden, T. L., Schaffer, A. A., Zhang, J., Zhang, Z., Miller, W., and Lipman, D. J. (1997) Gapped BLAST and PSI-BLAST: A new generation of protein database search programs. *Nucleic Acids Res. 25*, 3389–3402.
20. Edgar, R. C. (2004) MUSCLE: Multiple sequence alignment with high accuracy and high throughput. *Nucleic Acids Res. 32*, 1792–1797.
21. Crooks, G. E., Hon, G., Chandonia, J. M., and Brenner, S. E. (2004) WebLogo: A sequence logo generator. *Genome Res. 14*, 1188–1190.
22. Izard, T., and Sygusch, J. (2004) Induced fit movements and metal cofactor selectivity of class II aldolases: Structure of *Thermus aquaticus* fructose-1,6-bisphosphate aldolase. *J. Biol. Chem. 279*, 11825–11833.
23. Midelfort, C. F., Gupta, R. K., and Rose, I. A. (1976) Fructose 1,6-bisphosphate: Isomeric composition, kinetics, and substrate specificity for the aldolases. *Biochemistry 15*, 2178–2185.
24. Qamar, S., Marsh, K., and Berry, A. (1996) Identification of arginine 331 as an important active site residue in the class II fructose-1,6-bisphosphate aldolase of *Escherichia coli*. *Protein Sci. 5*, 154–161.
25. Alberts, I. L., Nadassy, K., and Wodak, S. J. (1998) Analysis of zinc binding sites in protein crystal structures. *Protein Sci. 7*, 1700–1716.
26. Williams, G. J., Domann, S., Nelson, A., and Berry, A. (2003) Modifying the stereochemistry of an enzyme-catalyzed reaction by directed evolution. *Proc. Natl. Acad. Sci. U.S.A. 100*, 3143–3148.
27. Schneider, T. D., and Stephens, R. M. (1990) Sequence logos: A new way to display consensus sequences. *Nucleic Acids Res. 18*, 6097–6100.

BI9001166